Numerical Simulation Of Electro-Thermo-Mechanical Phenomena During Resistance Sintering

S. BOURDON[1], V. BRUYERE[3], P. ROGEON[2], P. NAMY[3], C. DURAND[1], S. ROURE[1]

[1]SCHNEIDER ELECTRIC, EYBENS, France
[2]Univ. Bretagne Sud, IRDL, LORIENT, France
[3]SIMTEC, 5 rue Felix Poulat, GRENOBLE France

Introduction

Different silver based matrix composites, like Ag-C, Ag-WC or Ag-SnO$_2$, are involved in the manufacture of switches and circuit breakers as contact materials [1]. Optimizing the mechanical, electrical and thermal properties of these materials is of great importance for their reliability. To tailor the desired properties, metallic powders, with high thermal and electrical conductivity (Ag, or Cu), are mixed with a small amount of additive particles of micro/nanometer size [2, 3]. The size or the nature of these powder particles, can highly influence the physical properties of densified materials [3, 4]. Powder metallurgy techniques applied to those contact material mixes, combined with sintering can lead to the obtention of almost dense materials with optimized properties. Resistance Sintering (RS) is a fast sintering process providing high levels of densification within few seconds. Schneider Electric patented several years ago a specific process using RS, to sinter and bond cold-pressed contact material on metallic support in a single operation [5]. For the industrial applications, it is essential to be able to properly control the final shape and the relative density of these sintered contact commonly referred to as tip. To anticipate and better control those final properties, a numerical simulation of the RS process is investigated here for two contact materials AgC and AgWC. To be consistent, the numerical model takes into account the fully coupled electrical-thermal-mechanical phenomena [6, 7]. The mechanical behavior of the tip during RS is described with a modified Norton-Green law [8]. Creep and sintering tests have been achieved on a Gleeble machine to define specific laws for each contact materials to be implemented in the model. Furthermore, a specific attention is paid to the modelling of the electro-thermo-mechanical contact conditions between the tip and the sintering tool referred in the following as the electrode, which influences greatly the sintering kinetic [7].

Operating Conditions / Geometry

In order to sinter and compact the tip, a high current and a compression load are applied from the electrode to the sample (see Figure 1). to densify the material and to obtain the required metallurgical and mechanical properties. Several physical phenomena are involved in the process, leading to a complex multi-physics problem.

The geometry used for COMSOL Multiphysics® calculations is described schematically in Figure 1. A 2D axi-symmetry assumption is considered to simplify the problem without any loss of information. For each equation, the relevant symmetry boundary conditions are applied at the revolution axe.
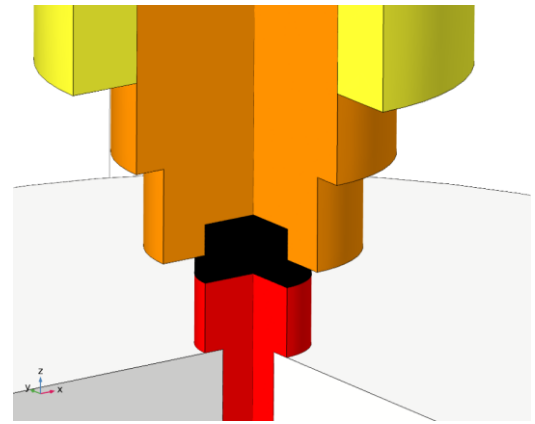
Figure 1: 2D axi-symmetrical geometry composed by the electrode (orange) and its holder (yellow), the sample (black) and the support (red and gray)

The full description of the different parts (electrode, sample, support…) including their properties are not provided due to confidentiality purpose. For the same reason, the geometrical dimensions have been made non-dimensional, as the different results presented in this work. Nevertheless, the whole modeling strategy is detailed here.

Governing Equations

Each "physics" used in COMSOL Multiphysics® is detailed with the different assumptions used in this work.

Electric Problem

The current conservation is solved by using the electric potential formulation:

$$\nabla \cdot [-\sigma_{elec}\nabla V] = 0 \qquad \textit{Eq. 1}$$

where V is the electric potential and σ_{elec} the electrical conductivity of the medium. The electric field $\boldsymbol{E}$ is equal to $-\nabla V$.

A transient inward current density is applied at the top of the electrode. The ground reference is set at the bottom of the geometry. Electrical contact conditions are defined at each interface to define the "electric potential jump" between the parts due to the imperfection of the contact. Indeed, at a microscopic level, contact is made at a finite number of spots defined by the local surface asperities. Furthermore, physico-chemical state of the surfaces may also modify the contact resistance. A global approach is used here by writing the following relations to link the normal electric current density at the upside and downside boundaries:

$$\boldsymbol{n} \cdot \boldsymbol{J_1} = \frac{1}{\rho_s}(V_1 - V_2)$$
$$\boldsymbol{n} \cdot \boldsymbol{J_2} = \frac{1}{\rho_s}(V_2 - V_1)$$

<div align="right">Eq. 2</div>

where $\boldsymbol{J_i} = \sigma \boldsymbol{E_i}$ is the electric current density at each side of the interface and ρ_s the contact resistance.

For each interface, the electrical contact resistance has been experimentally evaluated and then defined in the model through empirical data as functions of the temperature at a prescribed pressure. To take into account the irreversibility aspect of the contact resistance evolution with the temperature [9], a supplementary EDO is solved to evaluate the maximum temperature at each nodes. In a future work, relations with the maximum contact pressure will be provided and taken into account in the modeling.

Thermal Problem

Due to the high current flowing through the metallic pieces and the contact junctions between them, thermal energy is generated inside the media and at the interfaces. The Joule effect inside the parts is taken into account as a source term of the following energy equation:

$$\rho C_p \frac{\partial T}{\partial t} + \nabla \cdot [-k \nabla T] = \boldsymbol{J} \cdot \boldsymbol{E}$$

<div align="right">Eq. 3</div>

where T is the temperature, ρ the density, k the thermal conductivity and C_p the heat capacity of the material and the resistive heat source term in the right-hand side of the equation.

As for the electric formulation, contact resistances are defined through the thermal point of view with the following relations between the heat fluxes:

$$\boldsymbol{n} \cdot \boldsymbol{q_1} = h_s(T_2 - T_1) + \alpha \cdot \rho_s \cdot J_1^2$$
$$\boldsymbol{n} \cdot \boldsymbol{q_2} = h_s(T_1 - T_2) + (1 - \alpha) \cdot \rho_s \cdot J_2^2$$

<div align="right">Eq. 4</div>

where $\boldsymbol{q_i}$ is the heat flux defined as $-k_i \nabla T_i$, h_s is the contact conductance involved in the heat flux across the surfaces in contact, and α is the partition coefficient of the heat flux $(\rho_s \cdot J^2)$ generated by Joule effect in the electrical contact resistance ρ_s.

For each surface in contact, the heat conductance values are defined as functions of the temperature as are the electrical contact resistances (see previous section). The value of α is fixed at 0.5 [10].

Concerning the other thermal boundary conditions, a reference temperature is applied at the bottom of the system, far from the heated zone. Surface-to-Ambient radiative conditions are applied for exterior boundaries to take into account the radiative heat flux.

Mechanical Problem
In order to predict the stress and strain states in the sample, the equilibrium of mechanical forces is expressed by the following equation:

$$\nabla \cdot \sigma = 0$$

<div align="right">Eq. 5</div>

where σ is the stress tensor.

Based on the literature [11] and internal experimental results, a constitutive law considering the porosity of the contact material is used to describe the strain rate evolution:

$$\dot{\varepsilon} = \frac{1}{K^n} \frac{(\sigma_{eq} - \sigma_y)^n}{\sigma_{eq}} \times \left(\frac{3}{2} c \, \bar{s} + f \, I_1 \, \bar{I}\right)$$

<div align="right">Eq. 6</div>

where $I_1 = tr(\sigma_{ij})$ is the first invariant of the stress tensor, $J_2 = \frac{1}{2}\Sigma_{i,j} s_{i,j} s_{j,i}$ is the second invariant of the deviatoric stress tensor s ($s = \sigma - \left(I_1/3\right) I$), σ_y is the yield stress, K and n are the creep coefficients, and σ_{eq} the equivalent stress for the porous medium $\sigma_{eq} = \sqrt{f \, I_1^2 + 3 \, c \, J_2}$.

The relation (eq.6) is obtained from a classical Norton creep law [8], tuned with two functions c and f, related to the material density:

$$f(dr) = F1 \left(\frac{1 - dr}{dr - d_0}\right)$$

<div align="right">Eq. 7</div>

$$c(dr) = 1 + C1 \left(\frac{1 - dr}{dr - d_0}\right)$$

<div align="right">Eq. 8</div>

where F_1 and C_1 are two constants, d_0 is the initial density and dr is the density of the matter obtained with the following mass balance:

$$\frac{1}{dr} \frac{d}{dt}(dr) = -tr(\dot{\varepsilon})$$

<div align="right">Eq. 9</div>

If the conditions $(dr = 1)$, $f = 0$ and $c = 1$ are applied to the eq.6, we get back the classical Norton law.

A constant high pressure is imposed at the top of the electrode to press the sample. Moreover, a roller condition is applied at the bottom of the system to close the mechanical problem. Mechanical contact conditions are used for the boundaries of the sample, by computing the contact pressure as a function of the distance between the relevant contact surfaces.

This system of equations is implemented in COMSOL Multiphysics® and enriched with experimental data for different operating conditions. An external optimization loop has been used to characterize the mechanical constitutive law. Each

contact material property (thermal and electric conductivities, density) is described as a function of the temperature and relative density, except heat capacity, which varies only with temperature.

All these equations are thus strongly coupled together through the contact conditions as well as the variations of contact material properties as functions of temperature and relative density.

Numerical Aspects

Considering the several couplings and non-linearities, numerical aspects have to be carefully managed to guarantee the validity and the precision of the numerical results.

Mesh
A sensitivity study about the mesh properties has been performed to ensure no-dependency of the solution on the mesh. The retained mesh is shown in Figure 2, with a refinement at the contact boundaries:
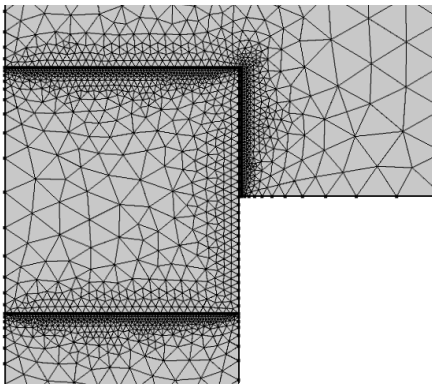

Figure 2: Mesh distribution

Contact Pairs
Contact pairs are defined to model the contact between the sample and the electrodes. Both methods available in COMSOL Multiphysics® (penalty method and augmented Lagrangian formulation) have been investigated to tackle this contact problem. By taking care of the mesh at the destination and source boundaries, both approaches lead to numerical convergence. The augmented Lagrangian formulation has finally been selected for a more precise and less "noisy" evaluation of the contact pressure.

Solvers
The BDF algorithm is selected as the time-dependent solver by carefully tuning the time-step and by using the "previous solution" feature to evaluate the temperature history. A fully coupled approach is adopted to solve this highly non-linear and strongly coupled problem. The damping factor is maintained at a low value (0.1) to ensure the numerical convergence under robust conditions.

The CPU time is roughly 1 hour with a PC of 2 processors and 32Go RAM for the entire cycle.

Simulation Results / Discussion

A study case is performed to evaluate the model prediction by comparison to experimental results. The duration of the applied current density is defined by τ and the load is applied during 4τ.

The electric potential is plotted in Figure 3 at two different instants, showing the electric potential jump between the contact interfaces due to contact resistances.
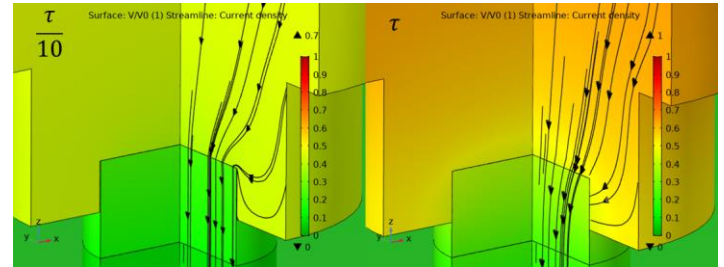

Figure 3: Non-dimensional electric potential and current density with streamlines at $t = \tau/10$ and $t = \tau$

In order to validate our approach, numerical and experimental differences of electric potential are confronted in Figure 4 (non-dimensional values for the electric potential, V). The order of magnitude and tendencies are obtained with the numerical approach. A more precise law could be calibrated in the future to model the contact resistances by taking into account more accurately the influence of the contact pressure.
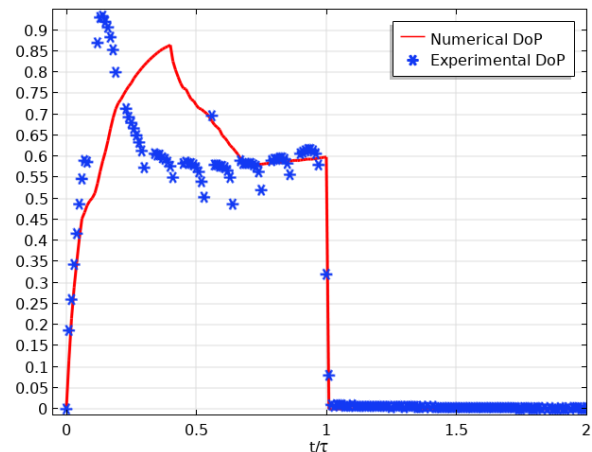

Figure 4: Non-dimensional Differences of electric potential (DoP) between two entities of the geometry obtained numerically (in red) and experimentally (in blue)

The temperature field is plotted for different instants in Figure 5. At the beginning ($t = \tau/4$), heat is mainly generated at the interface between the electrode and the sample due to a high contact resistance. The sample and the electrode are only in contact at the upper boundary. When the sample is pressed ($t > \tau/2$), it radially expands. The lateral contact with the electrode allows the electrical current to cross this interface (Figure 3, $t = \tau$), and leads also to a heat exchange by conduction. The contact pressure increases (magenta arrows in Figure 5), as well as the contact surface leading to an homogenization of the temperature in the sample.
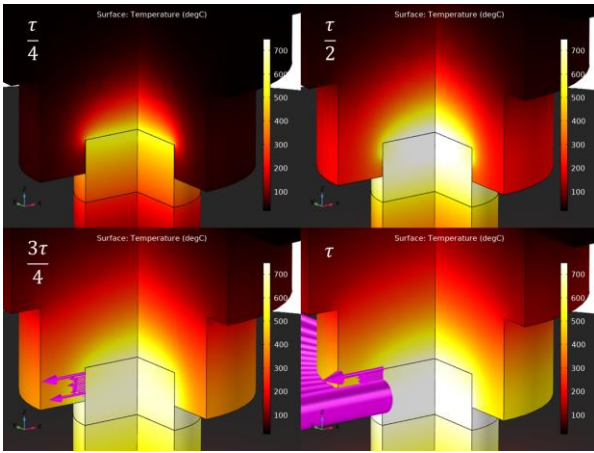
Figure 5: Temperature field (in color) and contact pressure (magenta arrows) at 4 instants

The temperature in the center of the sample is plotted in Figure 6 illustrating the fast temperature increase during the electric current application, as well as the cooling kinetic.
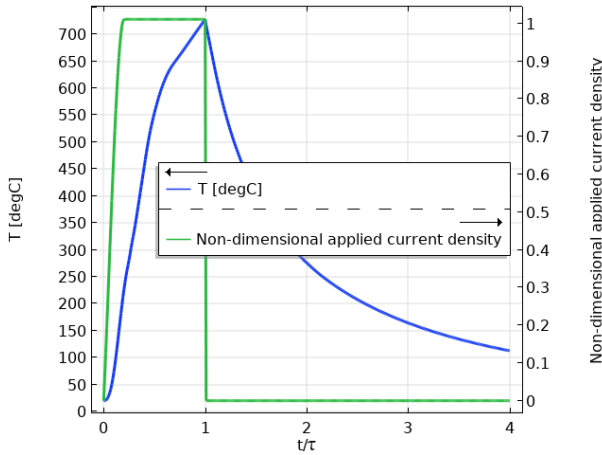
Figure 6: Temperature in the center of the sample (blue) and non-dimensional applied current density (green) as a function of time

In order to validate our numerical approach, numerical results are compared with experimental temperature measurements in different points of interest. An example of these comparisons is shown in Figure 7 for a point located at the upper electrode.
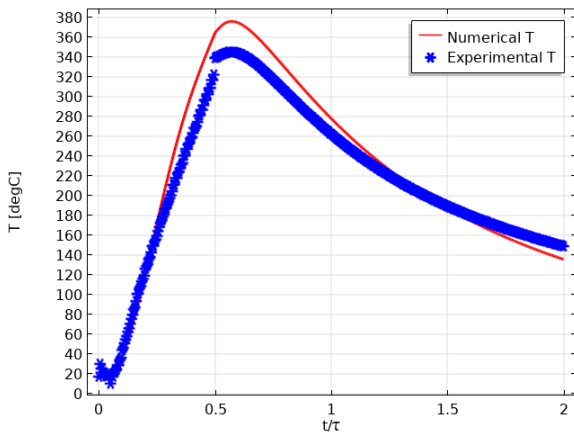

Figure 7: Comparison between experimental (blue) and numerical temperatures (red) at a point located in the electrode

Good agreement is obtained in Figure 7 for the temperature evolution both qualitatively and quantitatively, validating the assumptions used for the modelling.

To complete the comparison and the validation of the model, the mechanical aspects are also studied in details. Indeed, the aim of the model is to predict accurately the final dimensions of the sample and its mechanical and metallurgical state after sintering.

The evolution of the mean density is plotted in blue in Figure 8 as a function of time to illustrate the densification process. Due to high compressive stress and high temperature, the material is sintered and compacted during the period τ. After this period, the evolution of the density slightly increases and stays at a constant value.
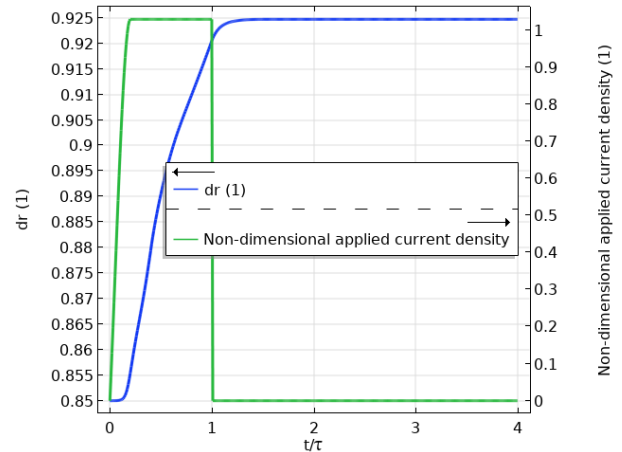
Figure 8: Mean density evolution (blue) and non-dimensional applied current density (green) as a function of time

The density distribution in the tip is shown at different instants in Figure 9, illustrating the compaction of the material during the process. Heterogeneities are observed, mainly due to the stress distribution heterogeneities in the sample.
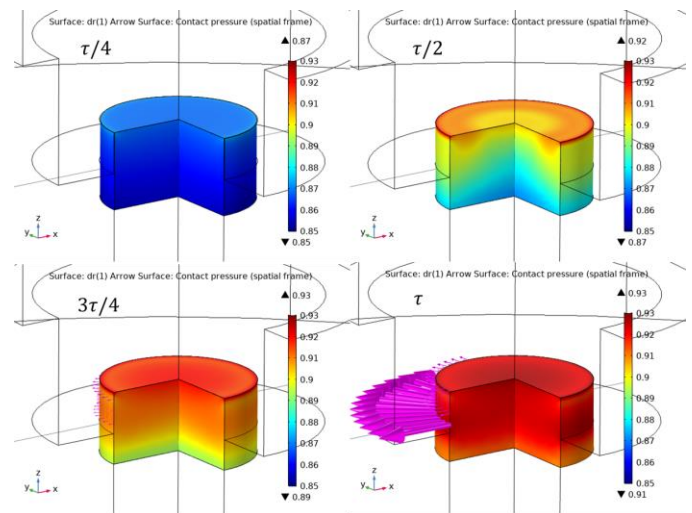
Figure 9: Density distribution in the tip (in color) and contact pressure (magenta arrows) at four instants

The vertical displacement, normalized by its minimal value, is plotted in Figure 10 as a function of time illustrating two different regimes under the pressure load. During the first period τ, the sample is strongly compressed. Then, when the temperature decreases, the densification is finished and shear deformations occur in this quasi-oedometric configuration. A stationary state is finally reached, leading to the final dimension of the sample. Indeed, after unloading, the dimension of the sample remains the same due to the weak elastic part of the strain tensor. The obtained dimensions of the sintered sample have finally been compared with experimental data giving very promising results.
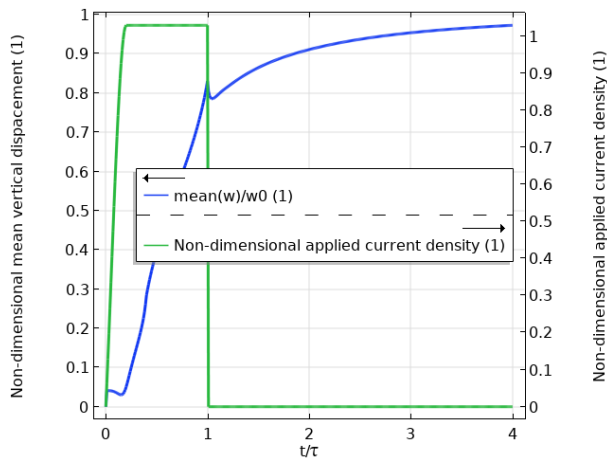
Figure 10: Mean vertical displacement evolution (blue) and non-dimensional applied current density (green) as a function of time

The equivalent stress is plotted in Figure 11 after unloading, emphasizing the residual stresses in the sample. The model can now be used through parametric studies to deeply understand the influence of each parameter on the resulting stress and strain states of the sample.
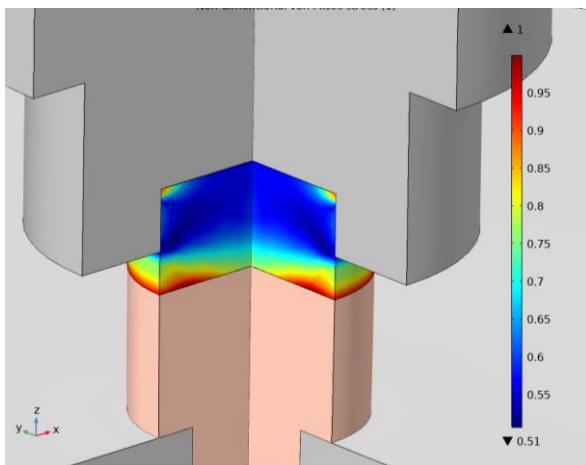
Figure 11: Non-dimensional equivalent stress in the sample at its final state after unloading

Conclusions

A numerical model has been developed in this work to deeply understand and precisely control the resistance sintering process. Electrical, thermal and mechanical phenomena have been considered to predict the final density and residual stresses in the sintered sample. Contact conditions have been thoroughly calibrated through experimental data to define electrical and thermal resistance at the interfaces between the different considered parts as a function of the temperature. The mechanical constitutive law has also been preciously calibrated with experimental work.

This complex and fully coupled multi-physics problem has been solved by adapting appropriately the numerical aspects. Confrontations with experimental measurements - differences of electric potential, temperatures and final dimensions of the sample - have been performed to validate the approach. Good agreements have been obtained for each "physics" involved (electrical, thermal and mechanical aspects). The model can now be used to define the optimized operating conditions leading to the process improvement.

References

1. J.L. Wintz, S. Hardy, (2013), Design guideline of contactors: Optimal use of assembled contacts, Holm Conference on Electrical Contacts (HOLM), IEEE 59th, p 1-6. https://doi.org /10.1109/HOLM.2014.7031014
2. O. E. Falodun, B. A Obadele, S. R. Oke, A. M. Okoro, P. A. Olubambi, (2019), Titanium-based matrix composites reinforced with particulate, microstructure, and mechanical properties using spark plasma sintering technique: a review, International Journal of Advanced Manufacturing Technology, https://doi.org/10.1007/s00170-018-03281-x
3. S. R. Oke, O. O. Ige1, O. E. Falodun, A. M. Okoro, M. R. Mphahlele, P. A. Olubambi, (2019), Powder metallurgy of stainless steels and composites: a review of mechanical alloying and spark plasma sintering, International Journal of Advanced Manufacturing Technology, https://doi.org/10.1007/s00170-019-03400-2
4. G. Li, H. Cui, J. Chen, X. Fang, W. Feng, J. Liu, (2017), Formation and effects of CuO nanoparticles on Ag/SnO2, J. Alloy Compd 696, 1228-1234. https://doi.org/10.1016/j.jallcom.2016.12.092
5. J.-P. Favre-Tissot, G. Février, J. Vanin. Contact électrique à pastille de contact frittée et son procédé de fabrication. Brevet FR2627894 (A1), 1 septembre 1989
6. K. Vanmeensel , A. Laptev, H. Sheng, I. Tkachenko, O. Van der Biest, J. Vleugels, (2013), Experimental study and simulation of plastic deformation of zirconia-based ceramics in a pulsed electric current apparatus, Acta Materialia 61 2376–2389
7. C. Manière, L. Durand, E. Brisson, H. Desplats, P. Carré, P. Rogeon, C. Estournès, (2017), Contact resistances in spark plasma sintering: From in-situ and ex-situ determinations to an extended model for the scale up of the process, Journal of the European Ceramic Society, Volume 37, Issue 4, April, Pages 1593-1605. https://doi.org/10.1016/j.jeurceramsoc.2016.12.010
8. C. Manière, U. Kus, L. Durand, R. Mainguy, J. Huez, D. Delagnes, C. Estournès, (2016), Identification of the Norton-Green Compaction Model for the Prediction of

the Ti–6Al–4V Densification During the Spark Plasma Sintering Process, Advanced Engineering Materials, Vol 18, Issue 10, p 1720-1727. https://doi.org/10.1002/adem.201600348

9. E. Geslain, P. Rogeon, T. Pierre, C. Pouvreau, L. Cretteur, (2018), Coating effects on contact conditions in resistance spot weldability, Journal of Materials Processing Technology, Volume 253, March 2018, Pages 160-167

10. P. Rogeon, R. Raoelison, P. Carre, F. Dechalotte, (2009), A microscopic approach to determine electro-thermal contact conditions during resistance spot welding process, Journal of Heat Transfer, Vol. 131, Issue 2, pp 022101.1-022101.11.

11. Abouaf, M. (1985). Modélisation de la compaction de poudres métalliques frittées Approche par la mécanique des milieux continus. PhD Thesis.